



Energy Exchanges between Density Fronts and Near-Inertial Waves Reflecting off the Ocean Surface

NICOLAS GRISOUARD

Department of Environmental Earth System Science, Stanford University, Stanford, California, and Department of Physics, University of Toronto, Toronto, Ontario, Canada

LEIF N. THOMAS

Department of Environmental Earth System Science, Stanford University, Stanford, California

(Manuscript received 10 April 2015, in final form 28 September 2015)

ABSTRACT

Inertial waves propagating upward in a geostrophically balanced front experience critical reflections against the ocean surface. Such reflections naturally create oscillations with small vertical scales, and viscous friction becomes a dominant process. Here, friction modifies the polarization relations of internal waves and allows energy from the balanced front to be exchanged with the ageostrophic motions and eventually dissipated. In addition, while in the well-known inviscid case internal waves propagate on only two characteristics, this study demonstrates using an analytical model that strong viscous effects introduce additional oscillatory modes that can exchange energy with the front. Moreover, during a linear, near-critical reflection, the superposition of several of these oscillations induces an even stronger energy exchange with the front. When the Richardson number based on the frontal thermal wind shear is $O(1)$, the rate of energy exchange peaks at wave frequencies that are near inertial and is comparable in magnitude to the energy flux of the incident, upward-propagating waves. Two-dimensional, linear numerical experiments confirm this finding. The analytical model also demonstrates that this process is qualitatively insensitive to the actual value of the viscosity or the form of the boundary condition at the surface. In fully nonlinear experiments, the authors recover these qualitative conclusions. However, nonlinear wave-wave interactions and turbulence in particular, strongly modify the amount of energy that is exchanged with the front. In practice, such nonlinear effects are only active when the incident waves have frequencies higher than the Coriolis frequency, since these configurations are conducive to near-resonant triad interactions between incident and reflected waves.

1. Introduction

Most of the ocean's kinetic energy is contained in the mesoscale eddy field (Ferrari and Wunsch 2009), with flows characterized by the hydrostatic and geostrophic balances. Such “balanced” motions tend to aggregate into larger scales, following an inverse cascade of energy. Energy dissipation on the other hand happens at much smaller scales, and understanding how energy in balanced motions is transferred to small scales is currently the subject of intense research. Ocean fronts are believed to host possible energy pathways for dissipating the mesoscale eddy field

(Capet et al. 2008; Molemaker et al. 2010; D'Asaro et al. 2011). An ocean front is characterized by large horizontal density gradients, strong vertical shear, and Rossby and Richardson numbers that can be of order one. In this case, the geostrophic balance is not overwhelmingly dominant and ageostrophic motions can arise that break the inverse cascade (Thomas et al. 2008; Capet et al. 2008).

One ageostrophic instability that is particularly effective at removing kinetic energy from geostrophic frontal flows is symmetric instability (SI). SI forms in the surface boundary layer of ocean fronts when the stratification is weakened by winds or sea-to-air heat transfer such that the Richardson number \bar{Ri} of the balanced flow is less than one (Haine and Marshall 1998; Taylor and Ferrari 2009; Thomas and Taylor 2010; Thomas et al. 2013). In the absence of destabilizing atmospheric forcing, SI rapidly restratifies the boundary layer,

Corresponding author address: Nicolas Grisouard, University of Toronto, Department of Physics, 60 St. George Street, Toronto, ON M5S 1A7, Canada.
E-mail: nicolas.grisouard@utoronto.ca

driving \overline{Ri} to one, thus extinguishing itself (Taylor and Ferrari 2009). At this stage, mixed layer instability (MLI), a type of baroclinic instability, takes over and further increases \overline{Ri} past one (Boccaletti et al. 2007; Fox-Kemper et al. 2008). MLI is primarily a balanced instability and does not result in the direct dissipation of frontal energy (Boccaletti et al. 2007; Callies et al. 2015). It is therefore not well understood how energy in balanced motions is dissipated for $Ri > 1$.

In this article, we explore a possible pathway for energy removal from fronts in the $\overline{Ri} > 1$ regime involving internal waves. Previous studies have shown that internal waves can be trapped by ocean fronts (e.g., Kunze and Sanford 1984; Kunze et al. 1995; Rainville and Pinkel 2004; Whitt and Thomas 2013; Joyce et al. 2013) and that they can exchange energy with them (Thomas and Taylor 2014). Internal waves in the ocean are usually generated by the winds and tides and are restored by the Coriolis force, characterized by the Coriolis frequency f , and by buoyancy forces, characterized by the buoyancy frequency $N = \sqrt{-(g/\rho_0)\partial_z \bar{\rho}}$. Here, g is the gravitational acceleration, ρ_0 is a constant reference density, and $\rho_0 + \bar{\rho}$ is the unperturbed density field. In an ocean front, however, the restoring force of internal waves is affected by the horizontal buoyancy gradient of the balanced flow, characterized by the quantity $S^2 = -(g/\rho_0)\partial_x \bar{\rho}$, where x is the across-front direction, and by the vertical shear in thermal wind balance, namely, $|S^2/f|$. This shear imparts a horizontal component to the absolute vorticity of the fluid and therefore modifies the effective Coriolis force (i.e., the advection of absolute momentum; Whitt and Thomas 2013).

These modifications to the restoring forces change the internal waves' propagation properties, including the characteristic angles along which their energy propagates (Mooers 1975; Whitt and Thomas 2013). In particular, internal waves of frequency f , or inertial waves, propagating in oceanic fronts can flux energy either horizontally, as in the classical limit, or on a slanted path. In Grisouard and Thomas (2015, hereinafter referred to as GT15), we studied a consequence of this property, which is that when waves of frequency f propagate upward (e.g., associated with a formerly superinertial wave that has propagated from a lower latitude; see section 7 in GT15 for additional examples) along the steep angle and encounter the flat ocean surface, they cannot reflect back down. This case is a singularity of the linear, inviscid theory since the reflected ray tubes become infinitely focused and the energy infinitely dense. In GT15, we called such a reflection critical by analogy with the critical reflection of classical internal waves against a wall, whose slope matches the wave characteristic slope (Phillips 1966; Thorpe and Haines 1987) or with the critical reflection of inertial waves against a horizontal boundary in the case

when the horizontal component of Earth's rotation vector cannot be ignored (Gerkema and Shrira 2005).

As we show in this article, critical and near-critical reflection of internal waves against the ocean surface result in an exchange of energy with fronts. First, in section 2, we review the propagation, reflection, and energetics of inviscid, steady-amplitude internal waves in fronts. In section 3, we introduce the propagation properties of steady-amplitude internal waves in fronts when viscous effects are taken into account. We also introduce a simplified linear analytical model, which highlights the role of viscous dissipation and of critical and near-critical reflections when exchanging energy with fronts. In section 4, we present numerical simulations, which are linear in the sense that we cancel all explicit advective terms to test the analytical predictions. In section 5, we discuss three effects that could potentially modify our conclusions, namely, the value of viscosity, the form of the boundary condition on the buoyancy, and nonlinear effects. While the first two effects do not qualitatively alter our conclusions, fully nonlinear simulations introduce new physics: wave–wave interactions and turbulence, which qualitatively modify the exchanges between the front and the ageostrophic motions. Conclusions and further insights are presented in section 6.

2. Inviscid internal waves in fronts

a. Critical, forward, and backward reflections

The configuration we consider is nearly identical to the one used by GT15: an idealized ocean front in geostrophic and hydrostatic balance, characterized by temporally and spatially uniform vertical and horizontal buoyancy gradients N^2 and S^2 , respectively. We orient the Cartesian coordinate axes such that z is the vertical coordinate, y is the alongfront direction, and x is the (horizontal) across-front direction. Alongfront velocities are permitted, but alongfront variations ($\partial_y \equiv 0$) are not permitted. We can write the density field as

$$\rho(x, z) = \rho_0 + \bar{\rho}(x, z) + \rho'(x, z, t), \quad (1)$$

where $\rho_0 + \bar{\rho}$ is the balanced frontal density field, and ρ' is the density perturbation. Because the ocean is characterized by $\bar{\rho} + \rho' \ll \rho_0$, we use the Boussinesq approximation. Geostrophy implies the existence of a thermal wind $\bar{v}(z)$ in the alongfront direction such that $\bar{v}_z = S^2/f$. Oceanic fronts are typically submesoscale features whose width is on the order of 10 km, allowing us to approximate f as a constant. The thermal wind shear is associated with a balanced Richardson number \overline{Ri} :

$$\overline{Ri} = f^2 N^2 / S^4, \quad (2)$$

and we assume that $\overline{\text{Ri}} > 1$, so that the flow is stable to symmetric instability. The features described so far will hereinafter be referred to as the “frontal flow.”

In the present article, internal waves are treated as perturbations relative to the balanced frontal flow. We only consider near-inertial waves, namely internal waves of frequency $\omega \approx f$, which justifies the use of the hydrostatic approximation, that is, $p_z = b$, where p is the scaled pressure anomaly, the lettered subscript denotes a partial derivative, and $b = -gp'/\rho_0$ is the buoyancy perturbation. When propagating in an inviscid medium in the absence of external forcing, the wave propagation is described by the Eliassen–Sawyer equation:

$$(f^2 + \delta_t^2)p_{zz} - 2S^2p_{xz} + N^2p_{xx} = 0. \quad (3)$$

We now consider a plane wave characterized by a wave vector $\mathbf{k} = (k, m)$, where $k = -\alpha m$, and m is the vertical wavenumber, described by the hydrostatic dispersion relationship of internal waves in fronts (GT15):

$$\Omega^2(\alpha) = f^2 + \alpha^2N^2 + 2\alpha S^2, \quad (4)$$

where Ω is the frequency. Signals characterized by α with an oscillating frequency $\omega = \Omega(\alpha)$ are plane, inviscid internal waves. As shown by, for example, Mooers (1975) or Whitt and Thomas (2013), the minimum wave frequency allowed by the dispersion relationship ω_m is lower than f , namely,

$$\omega_m = f\sqrt{1 - 1/\overline{\text{Ri}}}, \quad (5)$$

which is obtained when $\alpha = -S^2/N^2$, that is, when the phase lines, whose slopes are equal to α , run parallel to isopycnals,

Another consequence is that as $|S^2|$ increases, near-inertial wave energy can propagate along two characteristics with increasingly different slopes α_ω^+ and α_ω^- (Mooers 1975; Whitt and Thomas 2013). We hereinafter refer to them as steep and shallow, respectively, and by our definition, $|\alpha_\omega^+| > |\alpha_\omega^-|$. Crucially for inertial waves ($\omega = f$), Eq. (4) admits two solutions, namely, $\alpha_f^- = 0$ and $\alpha_f^+ = -2S^2/N^2$. This means that inertial waves propagating upward experience a critical reflection off the ocean surface, as documented in GT15. The critical reflection separates the frequency space into two regions: those of forward ($\omega > f$) and of backward ($\omega < f$) reflections, as illustrated in Fig. 1. Reflections are focusing (i.e., ray tubes shrink) when incident waves follow the steep (versus shallow) characteristics and defocusing otherwise. In the present work, we will only consider focusing reflections.

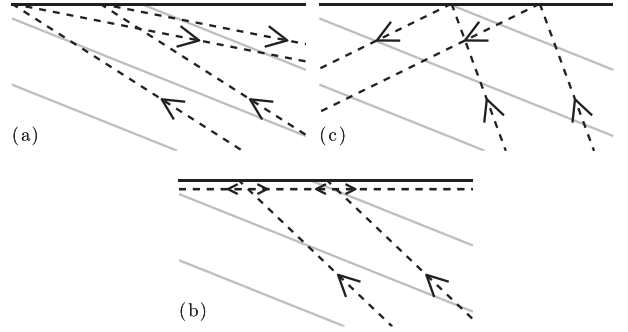


FIG. 1. Schematic of (a) backward ($\omega < f$), (b) critical ($\omega = f$), and (c) forward ($\omega > f$) reflections. Gray lines are unperturbed isopycnals, dashed lines are wave characteristics oriented along their associated direction of propagation.

b. Equations of motion and inviscid wave propagation

We now consider the following hydrostatic set of Boussinesq equations on an f plane:

$$D_t u - fv + p_x = 0, \quad (6a)$$

$$D_t v + fu + (S^2/f)w = 0, \quad (6b)$$

$$-b + p_z = 0, \quad (6c)$$

$$D_t b + S^2u + N^2w = 0, \quad \text{and} \quad (6d)$$

$$u_x + w_z = 0, \quad (6e)$$

where $D_t \equiv \partial_t + (\mathbf{u} \cdot \nabla)$ is the material derivative for the perturbations, and $\mathbf{u} = (u, v, w)$ is the velocity perturbations vector along with its Cartesian components. The perturbations are defined with respect to the frontal flow, hence the unusual presence of terms proportional to S^2 in Eqs. (6b) and (6d) (Mooers 1975; Whitt and Thomas 2013).

Internal waves induce perturbations in all u, v, w, b , and p fields, for which relative amplitudes of and phase differences between each field follow specific polarization relations. Assuming a freely propagating, plane, inviscid internal wave structure for the perturbations, namely,

$$(u, v, w, b) = \text{Re}\{P_0 \Pi_\omega^\pm \exp[i(-\alpha_\omega^\pm mx + mz - \omega t)]\},$$

where Re denotes the real part and P_0 is a reference pressure coefficient, and substituting this ansatz into Eqs. (6) yields

$$\Pi_\omega^\pm = \frac{im}{S^2 + \alpha_\omega^\pm N^2} \begin{bmatrix} i\omega \\ f + \alpha_\omega^\pm S^2/f \\ i\alpha_\omega^\pm \omega \\ S^2 + \alpha_\omega^\pm N^2 \end{bmatrix}. \quad (7)$$

From Eq. (7), we deduce that u and w oscillate in phase with each other and in quadrature with v and b .

c. Energetics of inviscid waves

We define the lateral average operator $\langle \cdot \rangle = (1/L) \int \cdot dx$, where L is the length of the domain, and assume that the domain is periodic in x . The laterally averaged evolution equation for the horizontal kinetic energy $\mathcal{K}_h = (u^2 + v^2)/2$, namely, $\langle [\text{Eq. (6a)}]u + [\text{Eq. (6b)}]v + [\text{Eq. (6c)}]w \rangle$, is

$$\langle \mathcal{K}_h \rangle_t + \langle (p + \mathcal{K}_h)w \rangle_z - \langle wb \rangle + S^2 \langle vw \rangle/f = 0. \quad (8)$$

The laterally averaged evolution equation for the available potential energy $\mathcal{P} = b^2/2N^2$, namely, $\langle [\text{Eq. (6d)}]b/N^2 \rangle$, is

$$\langle \mathcal{P} \rangle_t + \langle \mathcal{P} w \rangle_z + \langle wb \rangle + S^2 \langle ub \rangle/N^2 = 0, \quad (9)$$

and the mechanical energy $\mathcal{E}_h = \mathcal{K}_h + \mathcal{P}$ is described by

$$\langle \mathcal{E}_h \rangle_t + \langle (p + \mathcal{E}_h)w \rangle_z + S^2 \langle ub/N^2 + vw/f \rangle = 0. \quad (10)$$

Note that when nonlinear terms are ignored ($\mathbf{u} \cdot \nabla \equiv 0$), terms involving the advection of energy, that is, $\langle \mathcal{K}_h w \rangle_z$, $\langle \mathcal{P} w \rangle_z$, and $\langle \mathcal{E}_h w \rangle_z$, are absent from Eqs. (8)–(10).

The terms that quantify the exchanges between the internal waves and fronts are those proportional to S^2 . For the plane, inviscid internal waves described by Eq. (7), no energy exchange occurs, since u and w are in phase and in quadrature with v and b :

$$\langle ub \rangle = \langle vw \rangle = 0. \quad (11)$$

We now assume that two inviscid internal waves interfere. We further assume that those two waves participate in a linear reflection under the surface of the ocean and therefore share the same frequency ω and horizontal wavenumber k (Thorpe and Haines 1987; GT15). The solution for the streamfunction ψ (where $u = -\psi_z$ and $w = \psi_x$) is $\psi = \psi_0(\cos\varphi_1 - \cos\varphi_2)$ and satisfies $\psi|_{z=0} = 0$, where $\varphi_n = kx + m_n z - \omega t$, $m_1 = -k/\alpha_\omega^+$, and $m_2 = -k/\alpha_\omega^-$. Calculating u , v , w , and b from ψ and Eq. (7) yields

$$\frac{\langle vw \rangle}{f} = \frac{\psi_0^2 k}{2\omega} (m_2 - m_1) \sin(m_2 - m_1) z = -\frac{\langle ub \rangle}{N^2}, \quad (12)$$

that is, although there is a local exchange of kinetic energy between the front and the waves ($S^2 \langle vw \rangle/f \neq 0$), there is an equal and opposite exchange of available potential energy. Moreover, the local exchanges integrate vertically to zero. Therefore, inviscid internal waves cannot induce a net energy exchange in the problem considered.

3. Viscid internal waves in fronts

The previous section showed how the internal wave's inviscid polarization relations prevented energy exchange between the two-dimensional front and the waves. Such conclusions do not hold if waves dissipate and decay as they propagate. To illustrate this, and in order to keep calculations simple, we choose a vertical Laplacian as our frictional operator and lay out the basic physics governing the net transfer of energy from fronts to internal waves with steady amplitudes.

a. Wave solutions in the presence of friction

We assume that the perturbations are small enough to neglect the nonlinear interactions between perturbation modes (i.e., $\mathbf{u} \cdot \nabla \equiv 0$). We also consider a frictional operator $\mathcal{D} = \nu \partial_z^2$, with ν as both the vertical viscosity and buoyancy diffusivity (i.e., the Prandtl number is assumed equal to one), and a complex perturbation $\hat{p}(x, z, t) = \tilde{p}(z) \exp[i(kx - \omega t)]$, such that $p = \text{Re}[\hat{p}]$ (we define other quantities such as \hat{u} and \tilde{u} similarly). Under these conditions, frictional terms $\mathcal{D}\tilde{u}$, $\mathcal{D}\tilde{v}$, and $\mathcal{D}\tilde{b}$ now occupy the right-hand sides of Eqs. (6a), (6b), and (6d), respectively, to which we apply the differential operator $d_z \mathcal{L}_1$, with $d_z \equiv d/dz$ and $\mathcal{L}_1 \equiv i\omega + \nu d_z^2$, yielding

$$ik\mathcal{L}_1 \tilde{p}_z = f \mathcal{L}_1 \tilde{v}_z + \mathcal{L}_1^2 \tilde{u}_z, \quad (13a)$$

$$f \mathcal{L}_1 \tilde{v}_z = f^2 \tilde{u}_z - ikS^2 \tilde{u}, \quad \text{and} \quad (13b)$$

$$\mathcal{L}_1 \tilde{p}_{zz} = S^2 \tilde{u}_z - ikN^2 \tilde{u}, \quad (13c)$$

where \tilde{w}_z and \tilde{b} have been systematically replaced by $-ik\tilde{u}$ and \tilde{p}_z , respectively, following the continuity equation and hydrostatic balance. Substituting Eq. (13b) into Eq. (13a), applying the operator defined as $S^2 d_z - ikN^2$ to the result, and using Eq. (13c) to eliminate \tilde{u} yields the following equation for \tilde{p} :

$$\mathcal{L}_1 \mathcal{L}_2 \tilde{p} = C, \quad \text{with} \quad (14)$$

$$\mathcal{L}_2 = \nu^2 d_z^6 + 2i\nu\omega d_z^4 + (f^2 - \omega^2)d_z^2 - 2ikS^2 d_z - k^2 N^2.$$

Equation $\mathcal{L}_2 \tilde{p} = 0$ is the viscous equivalent of Eq. (3). The term C is a depth-invariant quantity, which we arbitrarily set to zero. Equation (14) has been derived for \tilde{p} . As Eq. (15) will show, using \tilde{v} or \tilde{b} would yield the same result, but using \tilde{u} , \tilde{w} , or $\tilde{\psi}$ would simply result in, for example, $\mathcal{L}_2 \tilde{u} = 0$, filtering out two solutions that are allowed by the full equations of motion.

Looking for solutions of Eq. (14) in the form of $\tilde{p} = \tilde{p}_0 e^{rz}$ yields eight roots r , which we refer to as r_n , $n = 1, \dots, 8$. In general, these roots can be written as $r_n = \delta_n + im_n$, with δ_n and m_n being real quantities. Two of

these roots are equal to $\pm\sqrt{\omega/\nu}$, while the other six roots are computed numerically. For every set of parameters used in this article, four δ_n are positive and four are negative, corresponding to solutions that decrease and increase with depth, respectively. Figure 2 shows, for a representative set of parameters, the vertical wavelengths $2\pi/m_n$. The two inviscid vertical wavelengths $-2\pi\alpha_\omega^+/k$ and $-2\pi\alpha_\omega^-/k$, the only ones allowed in the absence of viscosity, are also plotted for comparison. In particular, Fig. 2 shows that no vertical wavelength is equal to zero for any frequency displayed, which means that the singularity, predicted by the linear, inviscid theory for critical reflection is absent in the presence of viscosity, similar to the classical case (e.g., Dauxois and Young 1999).

In the example shown in Fig. 2, m_1 , indicated by the dashed purple line, corresponds to a wavenumber that closely satisfies the dispersion relation of the inviscid internal waves on the steep characteristic, while m_2 (denoted by a solid yellow line) corresponds to a wavenumber that satisfies the dispersion relation of the inviscid internal waves on the shallow characteristic only when viscous effects are weak, namely, when ω is significantly different than f . When $\omega \approx f$, the singular behavior on the shallow characteristic is prevented by viscous effects, and the inviscid dispersion relationship is not satisfied. In the case displayed in Fig. 2, $k < 0$ and the steep characteristic corresponds to a depth-increasing solution while the shallow characteristic corresponds to a depth-decaying solution. This corresponds to the configuration that we are considering, in which an incident wave propagates upward and the reflected waves propagate downward, with all waves decaying along their direction of propagation. Figure 3 includes a schematic of this configuration.

GT15 observed that during critical reflection, the reflected signal decays rapidly and resembles a standing wave in the vertical. Figure 2 shows that for $\omega = f$, $2\pi/m_2$, namely, the wavelength of the shallow characteristic solution that exists in the viscous limit, is mirrored by the equal and opposite wavelength $2\pi/m_3$, drawn as a solid orange line. When $\omega = f$, not only do these two solutions have equal and opposite vertical wavelengths, but the real parts of their roots happen to be approximately equal (not shown), allowing for a vertical standing wave-like pattern.

The two wavenumbers m_4 and m_6 (the solid and dashed blue lines in Fig. 2, respectively) correspond to the roots $r_4 = \sqrt{\omega/\nu}$ and $r_6 = -r_4$. For these roots, the time derivatives exactly cancel the viscous terms [i.e., $\mathcal{L}_1(e^{rz}) = 0$], and the corresponding equations of motion simplify to

$$-f\tilde{v} + ik\tilde{p} = 0, \quad -\tilde{b} + r\tilde{p} = 0, \quad \text{and} \quad (15a)$$

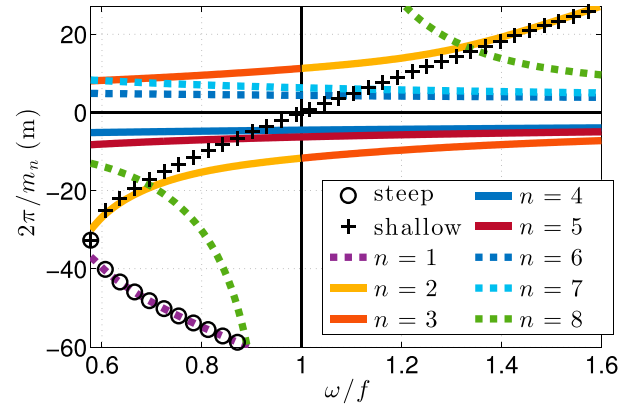


FIG. 2. Vertical wavelengths of internal waves in a front with (colored lines) and without (black crosses and circles) viscosity as a function of frequency. While the vertical wavelength shrinks to zero at $\omega = f$ on the shallow characteristic (black crosses) in the inviscid limit, it remains finite in the presence of viscous friction. Colored lines correspond to wavelengths $2\pi/m_n$, where m_n is the imaginary part of the roots of Eq. (14), and n is indicated in the legend as defined in section 3a. Richardson number $\overline{Ri} = 3/2$, and the left axis is located at ω_m/f . Other relevant parameters are $f = 10^{-4} \text{ s}^{-1}$, $N/f = 100$, $\nu = 5 \times 10^{-5} \text{ m}^2 \text{ s}^{-1}$, and $k = -1.57 \text{ km}^{-1}$. Solid (dashed) lines correspond to depth-decreasing (increasing) solutions. The same color scheme is used in Fig. 5.

$$f\tilde{u} + S^2\tilde{w}/f = 0, \quad S^2\tilde{u} + N^2\tilde{w} = 0, \quad ik\tilde{u} + r\tilde{w} = 0. \quad (15b)$$

According to the equations above, $(\tilde{v}, \tilde{b}, \tilde{p})$ are decoupled from (\tilde{u}, \tilde{w}) . In fact, for $\overline{Ri} \neq 1$, Eqs. (15b) cannot be satisfied simultaneously unless $\tilde{u} = \tilde{w} = 0$. We are left with the system of Eqs. (15a) whose solution is a geostrophic flow that oscillates at a near-inertial frequency.

Another wavenumber (m_5 ; solid burgundy line) approximately scales as the oscillating viscous boundary layer scale, namely, $r_5 \approx \sqrt{2i\omega/\nu}$. It is mirrored by a depth-increasing solution (m_7 ; dashed cyan line).

Finally, an eighth root r_8 (green dashed line) increases with depth. This root does not play any role in the configurations that we are considering.

b. Polarization relations

For simplicity, let us consider a single root r_n and its associated solution $(\tilde{u}_n, \tilde{v}_n, \tilde{w}_n, \tilde{b}_n) = \tilde{p}_n \boldsymbol{\Pi}_{\omega, \nu}^n e^{rz_n}$, with $r_n = \delta_n + im_n$. The polarization vector $\boldsymbol{\Pi}_{\omega, \nu}^n = (\boldsymbol{\Pi}_{\omega, \nu}^{n,u}, \boldsymbol{\Pi}_{\omega, \nu}^{n,v}, \boldsymbol{\Pi}_{\omega, \nu}^{n,w}, \boldsymbol{\Pi}_{\omega, \nu}^{n,b})$ becomes, using Eqs. (13) as well as the continuity and hydrostatic equations,

$$\boldsymbol{\Pi}_{\omega, \nu}^{n,u} = \frac{r_n^2(i\omega + \nu r_n^2)}{r_n S^2 - ikN^2}, \quad \boldsymbol{\Pi}_{\omega, \nu}^{n,w} = \frac{kr_n(i\omega + \nu r_n^2)}{i(r_n S^2 - ikN^2)}, \quad \text{and} \quad (16a)$$

$$\boldsymbol{\Pi}_{\omega, \nu}^{n,v} = \frac{1}{f} \left[ik - \frac{r_n^2(i\omega + \nu r_n^2)^2}{r_n S^2 - ikN^2} \right], \quad \boldsymbol{\Pi}_{\omega, \nu}^{n,b} = r_n. \quad (16b)$$

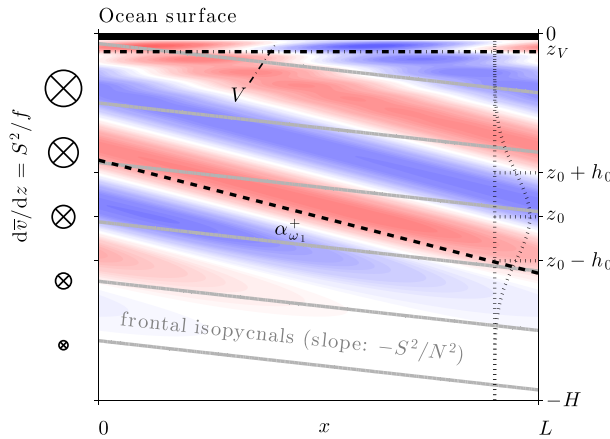


FIG. 3. Schematic of the flow configuration used in this study: frontal isopycnals (gray) and (left) geostrophic flow \bar{v} , domain boundaries, envelope of the wave maker (introduced in section 4a,) and wave field. The wave field in colored shades (field and color axis range arbitrary) consists of an incident wave radiating from the wave maker and the corresponding forward-reflected wave near the surface, both subject to viscous decay as they propagate. The incident wave corresponds to an internal wave with group velocity directed along the steep characteristic $\alpha_{\omega_1}^+$ (dashed line). The control volume V introduced in section 3c is sketched on top, along with its lower boundary at $z = z_V$ (horizontal dashed-dotted line). The wave maker introduced in section 4a is centered around z_0 and extends over a distance h_0 (dotted horizontal lines), and its envelope is drawn as the bell-shaped, dotted line.

The equations above show that the quadrature between u , w and v , b that was featured in Eq. (7) is lost, allowing for a net exchange of energy between internal waves and the front.

c. Viscous reflection against a horizontal boundary

We now consider the case of a reflection, which is essentially a case of interfering, dissipating waves, with the addition that critical and near-critical reflections intensify viscous effects and generate solutions to Eq. (14) that are not described by either the inviscid steep or shallow characteristics. In the absence of nonlinear effects, fluid motions are a linear combination of the solutions of Eq. (14):

$$(\tilde{u}, \tilde{v}, \tilde{w}, \tilde{b}) = \sum_{n=1}^8 \tilde{p}_n \mathbf{\Pi}_{\omega, \nu}^n \exp(r_n z), \quad (17)$$

where $\mathbf{\Pi}_{\omega, \nu}^n$ is the polarization vector for the solution n [cf. Eqs. (16)], and \tilde{p}_n is a weight corresponding to the surface pressure anomaly associated with each solution.

As explained previously, during a reflection, the only depth-increasing solution that we have to retain is $n = 1$, which corresponds to the incident wave for our configuration (e.g., Fig. 3). All signals created by the reflection

have to decrease with depth; thus, the three other depth-increasing solutions ($n = 6, 7, 8$) can be discarded. The other solutions we retain are therefore the viscosity-modified reflected wave ($n = 2$) as well as the solutions $n = 3, 4, 5$. Constraining the coefficients \tilde{p}_n in Eq. (17) requires knowledge of the boundary conditions. In this section, we consider the free slip and no normal flow boundary conditions at the ocean surface:

$$d_z \tilde{u}|_{z=0} = 0, \quad d_z \tilde{v}|_{z=0} = 0, \quad \text{and} \quad (18)$$

$$\tilde{w}|_{z=0} = 0 \quad \text{and} \quad \tilde{b}|_{z=0} = 0. \quad (19)$$

The boundary condition on the buoyancy in Eq. (19) was chosen because it is imposed by the numerical code we will use in section 4 (Winters et al. 2004) and corresponds to a fixed density gradient at the surface. This is somewhat unphysical since one would expect density perturbations to be advected along the boundary. As we will discuss in section 5b, opting for a no flux boundary condition on buoyancy changes the solution only quantitatively and leaves our main conclusions intact. Using Eqs. (16) and (17), Eqs. (18) and (19) become

$$\sum \tilde{u}_n r_n = 0, \quad \sum \tilde{v}_n r_n = 0, \quad \sum \tilde{w}_n = 0, \quad \sum \tilde{b}_n = 0, \quad (20)$$

with $\tilde{u}_n = \tilde{p}_n \Pi_{\omega, \nu}^{n, u}$, and so on, and the sums run from $n = 1$ to 5. These equations form a linear system of four equations and four unknowns (\tilde{p}_n , $n = 2, \dots, 5$) since we can assume, without loss of generality, that the incoming wave is known and that $\tilde{p}_1 = 1$. This system is solved numerically. Figure 4 shows an example of the buoyancy perturbation b and its components $\text{Re}[\tilde{b}_n] = \text{Re}[\tilde{b}_n \exp(r_n z + ikx)]$, $n = 1, \dots, 5$, for a critical reflection.

The excitation of these extra viscous solutions (i.e., with $n > 2$) is inherent to near-critical reflections. Because this case is where the focusing of the reflected wave is the strongest, it is also where viscous effects are the most active. We illustrate this fact in Fig. 5, which shows the buoyancy coefficients \tilde{b}_n normalized by the coefficient of the incoming wave as a function of frequency. The viscous solutions tend to zero away from $\omega = f$, while $n = 2$ (the reflected wave) is the only one (apart for the incident wave $n = 1$) active for frequencies away from critical reflection. As we will see next, the energy exchanges between the front and the waves are maximum where these viscous solutions are active.

d. Energy exchanges with the front

To quantify the energy exchange between the front and the waves, we construct an energy budget by integrating Eq. (10) over an appropriate control volume V .

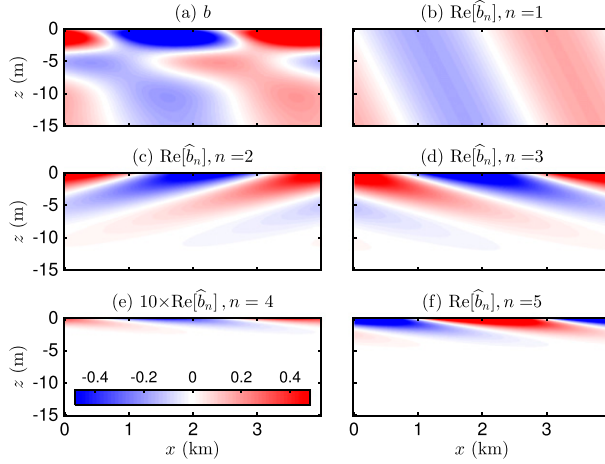


FIG. 4. Analytically computed buoyancy perturbation $b/\max(b)$ for (a) a critical reflection ($\omega = f$) and (b)–(e) its breakdown into the contributions from the various roots r_n , that is, $\text{Re}[\tilde{b}_n \exp(r_n z + ikx)]/\max(b)$ (all axes and color scales are identical). Note that the solution $n = 4$ had to be multiplied by 10 to be visible. This calculation has been made with $\bar{Ri} = 1.05$, $f = 10^{-4} \text{ s}^{-1}$, $N/f = 100$, $\nu = 5 \times 10^{-5} \text{ m}^2 \text{ s}^{-1}$, and $k = -1.57 \text{ km}^{-1}$.

After preliminary steps in which we retrieve the weight \tilde{p}_n of each solution by plugging Eq. (17) into Eqs. (20), deducing u , v , w , and b , and then deducing the exchange terms $S^2 \langle ub \rangle / N^2$ and $S^2 \langle vw \rangle / f$, we do as follows:

- 1) define a volume V bounded at the top by the ocean surface, from the bottom by a horizontal line located at z_V , and unbounded in the horizontal direction (see Fig. 3);
- 2) compute the laterally averaged kinetic, available potential and mechanical energy exchanges between the perturbations and the front within V :

$$\text{KX} = \frac{S^2}{f} \int_0^{z_V} \langle vw \rangle dz, \quad (21a)$$

$$\text{PX} = \frac{S^2}{N^2} \int_0^{z_V} \langle ub \rangle dz \quad \text{and} \quad (21b)$$

$$\text{EX} = \text{KX} + \text{PX}; \quad (21c)$$

- 3) compute the laterally averaged energy flux of the incident wave through $z = z_V$:

$$\text{EF} = (1/2) \text{Re} \langle \hat{p}_1 \hat{w}_1^* \rangle|_{z=z_V}; \quad (22)$$

- 4) and, finally, compute

$$R_{\mathcal{K}} = \text{KX}/\text{EF}, \quad (23a)$$

$$R_{\mathcal{P}} = \text{PX}/\text{EF} \quad \text{and} \quad (23b)$$

$$R_{\mathcal{E}} = R_{\mathcal{K}} + R_{\mathcal{P}}, \quad (23c)$$

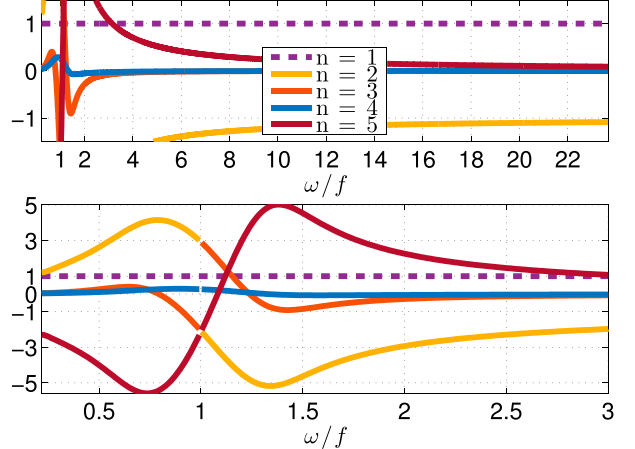


FIG. 5. Relative contributions of the individual roots to the total solution as a function of frequency, measured using the solution for the buoyancy perturbations at the surface. The quantities $\text{Re}[\tilde{b}_n / \tilde{b}_1]$ are analytically computed and normalized by the surface buoyancy perturbations induced by the incoming wave. The same line colors and styles of Fig. 2 are used here. Both panels show the same curves and only the axis ranges differ, highlighting the behavior for (top) $\omega/f \gg 1$ [(bottom) $\omega/f = O(1)$]. The same flow parameters as in Fig. 4 are used. The number of roots that contribute significantly to the total solution is largest for near-inertial frequencies and near-critical reflection. For $\omega \gg f$, only the incident ($n = 1$) and reflected ($n = 2$) waves contribute to the solution, as in the inviscid limit.

hereinafter referred to as the “exchange ratios,” to compare the rate of energy exchanged with the front to how much energy is influxed by the incident waves. For the calculation, we choose the following set of parameters identical to those used in Figs. 4 and 5: $\bar{Ri} = 1.05$, $f = 10^{-4} \text{ s}^{-1}$ (typical of midlatitudes), $k = -1.57 \text{ km}^{-1}$ (i.e., $2\pi/|k| = 4 \text{ km}$), and $N/f = 100$. This set of parameters for the frontal flow is representative of the Gulf Stream (see, e.g., Thomas et al. 2013). We also choose $\nu = 5 \times 10^{-5} \text{ m}^2 \text{ s}^{-1}$ and $z_V = -25 \text{ m}$.

Figures 6a and 6b display the various exchange ratios and show that with this parameter set, waves extract energy from the front during near-critical reflections, over a band of frequencies that correspond to where the reflected signal is strongly influenced by viscosity, as shown by Figs. 2 and 5. In addition, Fig. 6a shows that

$$R_{\mathcal{P}} > 0, \quad R_{\mathcal{K}} < 0 \quad \text{and} \quad |R_{\mathcal{P}}| > |R_{\mathcal{K}}|, \quad (24)$$

meaning that potential and kinetic energy transfers have opposite signs, with the transfer of potential energy from the front to the perturbations being more important in magnitude than the transfer of kinetic energy from the perturbations to the front, resulting in a net transfer of energy from the front to the perturbations. For

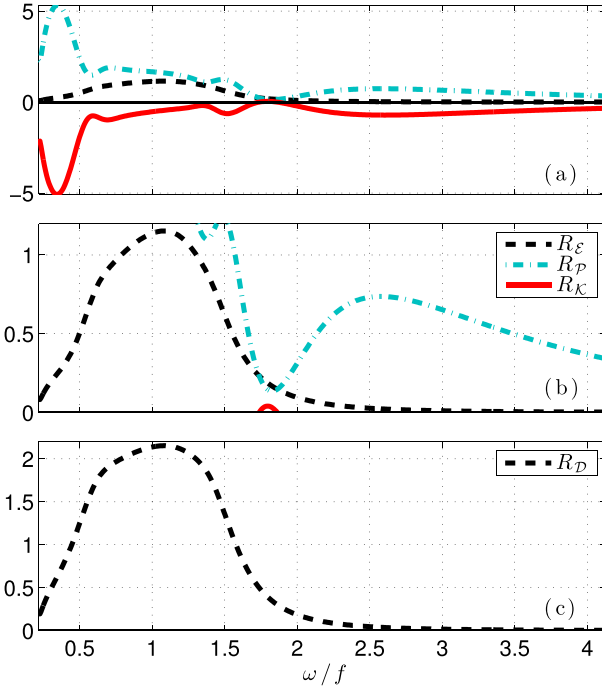


FIG. 6. (a),(b) The rate of kinetic $R_{\mathcal{K}}$, potential $R_{\mathcal{P}}$, and mechanical $R_{\mathcal{E}}$ energy extracted from the front and (c) the rate of dissipation of energy $R_{\mathcal{D}}$, computed analytically in the control volume V shown in Fig. 3, all normalized by the energy flux of the incident wave. For example, a value of $R_{\mathcal{P}} = +1$ means that within the control volume V , the front loses the available potential energy at the same rate as the energy that is being fluxed in by the waves through the base of V . Quantities are calculated with the same parameters as in Fig. 4 but as a function of ω/f . The same quantities are plotted in (a) and (b), but the ranges of the vertical axes are different.

frequencies away from f , however, $R_{\mathcal{K}}$ and $R_{\mathcal{P}}$ tend to cancel; thus, the net mechanical energy exchange rate $R_{\mathcal{E}}$ goes to zero.

The energy extracted from the front is mostly dissipated. To quantify this, we compute the volume integral of the dissipation

$$\text{ED} = \nu \int_0^{z_V} \langle \mathbf{u}_h \cdot \partial_z^2 \mathbf{u}_h + b \partial_z^2 b / N^2 \rangle dz \quad (25)$$

and normalize it by the incident energy flux:

$$R_{\mathcal{D}} = \text{ED}/\text{EF}, \quad (26)$$

hereinafter referred to as the “dissipation ratio.” We plot the result in Fig. 6c. Note that the sign conventions for EX and ED are opposite. We see that when energy is extracted from the front, the dissipation ratio can be greater than one, especially for frequencies close to f . Here, the amount of dissipation is therefore equal to the dissipation of the incoming wave (i.e., the incoming energy flux), augmented by an amount of the same order, whose source can only be energy extracted from the front.

The energy exchanges computed so far are the result of several interactions between individual wave solutions and do not give specific information as to whether a few specific interactions carry most of the exchanges, and if they do, which ones. We retrieve this information by breaking down the exchange terms into their individual components:

$$S^2 \langle ub \rangle / N^2 = \frac{1}{2} \sum_n \sum_q \text{Re} [\chi_{nq}^{\mathcal{P}}(z)], \quad \text{and} \quad (27a)$$

$$S^2 \langle vw \rangle / f = \frac{1}{2} \sum_n \sum_q \text{Re} [\chi_{nq}^{\mathcal{K}}(z)], \quad (27b)$$

where all indices are summed from 1 to 5 and with:

$$\chi_{nq}^{\mathcal{P}}(z) = (S^2 \tilde{u}_n \tilde{b}_q^*/N^2) \{ \exp[(r_n + r_q^*)z] \}, \quad (28a)$$

$$\chi_{nq}^{\mathcal{K}}(z) = (S^2 \tilde{v}_n \tilde{w}_q^*/f) \{ \exp[(r_n + r_q^*)z] \}. \quad (28b)$$

We then proceed to break down EX as well into the energy exchanges EX_{nq} due exclusively to the interaction between the solutions n and q :

$$\begin{aligned} \text{EX}_{nq} &= \frac{1}{2} \beta_{nq} \int_0^{z_V} \text{Re} [\chi_{nq}^{\mathcal{P}}(z) + \chi_{qn}^{\mathcal{P}}(z) + \chi_{nq}^{\mathcal{K}}(z) + \chi_{qn}^{\mathcal{K}}(z)] dz, \\ &\quad (29) \end{aligned}$$

where $\beta_{nq} = 1/2$ if $n = q$ and 1 otherwise, in order to avoid double counting the self-interaction terms. All of the terms in Eq. (29) are plotted as a function of the indices n and q in Fig. 7, which illustrates how the interactions between the different solutions act to exchange energy with the front. The interaction between the $n = 3$ and $n = 5$ solutions dominates the net energy exchange, although several other interactions play a nonnegligible role as well.

4. Numerical simulations

We now test our analytical model with numerical simulations.

a. Numerical model and setup

We use a modification of the numerical model of Winters et al. (2004), a pseudospectral, nonlinear, nonhydrostatic code solving the Boussinesq equations of motion. We simulate cases of critical, forward, and backward reflections, using the configuration schematized in Fig. 3 and vary S^2 and the forcing frequency ω_1 in our numerical simulations. Half of our experiments are fully nonlinear, while the other half are linear yet retain the interactions between the front and the waves [terms proportional to S^2 in Eqs. (6)] but do not allow for wave–wave interactions.

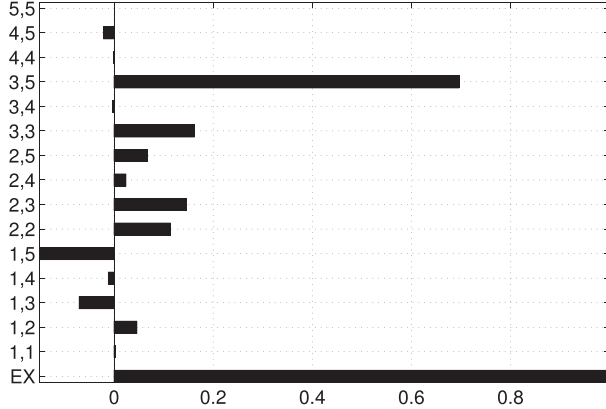


FIG. 7. Relative contributions of each individual exchange ratio EX_{nq} to EX , with n and q indicated on the vertical axis and normalized by their sum, namely, EX . A positive value represents a net transfer of energy away from the front, induced solely by all the interactions between solutions indexed by n and q , integrated vertically between the surface and the bottom of the control volume at $z = z_V$.

Each experiment is identified with a label starting with 1, 2, or 4 corresponding to $\overline{\text{Ri}} = 1.05$, 2, or 4, respectively, followed by the letter L (linear experiment) or N (fully nonlinear experiment) and ending with three digits corresponding to 10γ , where γ is a nondimensional measure of the frequency defined as $\gamma = (\omega_1 - \omega_m)/(f - \omega_m)$, with $\gamma = 0$ for $\omega = \omega_m$ and $\gamma = 1$ for $\omega = f$, that is, critical reflection. For example, the numerical experiment labeled 1N017 corresponds to a fully nonlinear experiment with $\overline{\text{Ri}} = 1.05$ and $\gamma = 1.7$. To generate the incident waves, we add a set of forcing terms, which we call the wave maker, to the right-hand sides of Eqs. (6a)–(6d). The wave maker is designed to generate a plane wave that propagates upward on the steep characteristic, with relative amplitudes and phases for each component that satisfy the polarization relations of inviscid inertia-gravity waves. Varying $\overline{\text{Ri}}$ and γ induces variations in wave quantities such as time scales, vertical propagation speeds, vertical viscous decay scales, or nonlinear activity. Therefore, the wave maker amplitude has to be varied, as well as the domain height H (together with n_z , the number of vertical levels), the time step Δt , and the integration duration ΔT (normalized by $T_{\omega_1} = 2\pi/\omega_1$, the forcing period). Table 1 displays all values used in the simulations, which we explain below, and we also refer the reader to Fig. 3, which illustrates some of the elements we are about to describe.

The domain has a horizontal length $L = 4\text{ km}$, discretized into $n_x = 256$ points, which corresponds to a horizontal resolution of $\Delta x \approx 15.6\text{ m}$. The vertical resolution is the same for all experiments, namely, $\Delta z \approx 48.8\text{ cm}$, but the depth H can take three different values, namely, $H = 500$, 1000, and 2000 m, corresponding to

TABLE 1. List of parameters used in the numerical experiments. X is a placeholder in the experiment label for N or L, and the values of ω_1/f are rounded.

Label	ω_1/f	$A (\text{m}^2 \text{s}^{-3})$	$H (\text{m})$	$\Delta t (\text{s})$	$\Delta T/T_{\omega_1}$
1X001	0.30	4.8×10^{-9}	500	50	20
1X003	0.45	9.0×10^{-9}	500	50	20
1X005	0.61	1.3×10^{-8}	500	50	20
1X008	0.84	2.1×10^{-8}	500	50	20
1X010	1	2.8×10^{-8}	500	50	20
1X013	1.2	4.2×10^{-8}	500	50	20
1X015	1.4	5.5×10^{-8}	500	50	32
1X017	1.6	7.0×10^{-8}	1000	50	25
1X020	1.8	9.9×10^{-8}	1000	50	25
1X030	2.6	2.6×10^{-7}	2000	25	20
1X036	3.0	4.3×10^{-7}	2000	10	20
1X050	4.1	1.1×10^{-6}	2000	5	20
2X002	0.77	1.9×10^{-9}	500	50	30
2X003	0.80	2.6×10^{-9}	500	50	30
2X005	0.85	4.1×10^{-9}	500	50	30
2X008	0.94	6.9×10^{-9}	500	50	20
2X010	1	9.1×10^{-9}	500	50	20
2X015	1.2	1.6×10^{-8}	500	50	20
2X020	1.3	2.5×10^{-8}	500	50	20
2X025	1.4	3.7×10^{-8}	1000	50	20
2X030	1.6	5.1×10^{-8}	1000	10	20
2X035	1.7	6.8×10^{-8}	1000	10	20
2X050	2.2	1.4×10^{-7}	1000	5	20
2X078	3.0	4.1×10^{-7}	1000	5	20
2X140	4.8	2.1×10^{-6}	2000	5	20
4X003	0.91	1.2×10^{-9}	500	50	60
4X005	0.93	1.6×10^{-9}	500	50	50
4X008	0.97	2.1×10^{-9}	500	50	50
4X010	1	2.5×10^{-9}	500	50	30
4X015	1.1	3.7×10^{-9}	500	50	30
4X020	1.1	5.2×10^{-9}	500	50	25
4X030	1.3	9.5×10^{-9}	500	50	20
4X040	1.4	1.6×10^{-8}	500	10	20
4X050	1.5	2.4×10^{-8}	500	10	20
4X070	1.8	5.0×10^{-8}	1000	10	20
4X100	2.2	1.1×10^{-7}	1000	10	20
4X200	3.6	6.7×10^{-7}	2000	5	20
4X300	4.9	2.2×10^{-6}	2000	5	20

$n_z = 1025$, 2049, and 4097 points, respectively. Because we have not implemented any sponge layer to absorb downward-propagating waves, the purpose of varying the domain depth is to prevent waves from reaching the bottom, reflecting off of it, and propagating back to the portion of the domain that interests us, namely, the top 100 m.

The Coriolis parameter is $f = 10^{-4}\text{ s}^{-1}$ and $N/f = 100$. When varying $\overline{\text{Ri}}$ to 1.05, 2, and 4, we effectively vary the background lateral gradient, that is, $S^2 \approx 9.8 \times 10^{-7}$, 7.1×10^{-7} , and $5.0 \times 10^{-7}\text{ s}^{-2}$, respectively. We ignore the modification of the wave physics by the horizontal component of Earth's rotation vector (Colin de Verdière 2012; Whitt and Thomas 2013), as they are negligible for the parameter regimes that we are considering (appendix B of GT15).

The domain is periodic in the x direction, and the following boundary conditions are imposed:

$$w|_{z=0} \equiv 0, \quad (30a)$$

$$(u_z, v_z + \bar{v}_z)|_{z=0} \equiv (0, 0) \Rightarrow v_z|_{z=0} \equiv -S^2/f, \text{ and} \quad (30b)$$

$$b|_{z=0} \equiv 0. \quad (30c)$$

The condition for v requires a surface stress in order to compensate for what Thomas and Rhines (2002) call the “geostrophic stress,” namely, the stress induced by the thermal wind shear. Our implementation of this stress is identical to that of GT15. Note that this stress was absent in section 3 since we were only interested in oscillating solutions.

The frictional operator is $\mathcal{D} = \nu \partial_z^2 - \nu_4 \partial_x^4$, with $\nu = 5 \times 10^{-5} \text{ m}^2 \text{s}^{-1}$ for the vertical viscosity and $\nu_4 = 5000 \text{ m}^4 \text{s}^{-1}$ for the horizontal biharmonic hyperviscosity. The terms ν and ν_4 are the same for both the momentum and buoyancy. The only purpose of the horizontal biharmonic operator is to keep the nonlinear simulations stable and it does not play any prominent role in the dynamics.

The implementation of the wave maker is described in detail in GT15, the key characteristics of which we summarize here. The wave maker consists of the following set of terms that we add to the right-hand sides of Eqs. (6a) and (6b):

$$(\mathbf{F}, F_4) = \Phi(z, t) \operatorname{Re}\{\Pi_{\omega_1}^+ \exp[i(k_1 x + m_1 z - \omega_1 t)]\}, \quad (31)$$

where $k_1 = -\alpha_{\omega_1}^+ m_1 = -2\pi/L$ and $\Phi(z, t) = A[1 - \exp(-ft)] \exp[-(z - z_0)^2/h_0^2]$. The amplitude A is adjusted for each experiment so as to ensure that the incident wave has an $O(0.1)$ Froude number $|m_1 U_1/N|$, with U_1 as the amplitude of the along- x velocity of the incident wave. Finally, $z_0 = -250 \text{ m}$ and $h_0 = 60 \text{ m}$.

The code uses a third-order Adams–Bashforth time-stepping scheme with a time step Δt and a duration of integration ΔT varying for each experiment (cf. Table 1). As explained in Winters et al. (2004), the code does not have a pressure solver since p is algebraically computed and substituted into the right-hand side forcing terms of the momentum equations.

b. Linear results

We run a set of simulations for which all wave–wave interactions are prohibited ($\mathbf{u} \cdot \nabla \equiv 0$) that allow us to test the analytical model of section 3 directly. We apply the procedure described in section 3d to our numerical experiments, namely, we calculate the exchange ratio

$R_{\mathcal{E}}$ [Eq. (23c)] as a function of ω_1 and $\overline{\text{Ri}}$. To compute EF [Eq. (22)], we isolate the incident wave by use of a filter in time and space (see GT15, their appendix C, for details). Our filter in time is made over two incident wave periods. Increasing this duration does not generate meaningful differences. We also average KX, PX, EX, and ED [Eqs. (21) and (25)] over the same duration.

We plot $R_{\mathcal{E}}$ in Fig. 8a and compare it with the prediction provided by our analytical model. Except for the lowest frequency simulated in the $\overline{\text{Ri}} = 1.05$ case, and a slight overestimation of the peak value of $R_{\mathcal{E}}$ in general, the results from the numerical and analytical solutions agree quite well. The enhancement of the exchanges around the critical reflection is stronger for low $\overline{\text{Ri}}$ since critical reflections are stronger for lower $\overline{\text{Ri}}$ (GT15).

We also verify that most of the energy extracted from the front by the perturbations is dissipated. Comparing Figs. 8a and 8b shows that whenever $R_{\mathcal{E}}$ is nonzero, $R_{\mathcal{D}}$ [Eq. (26)] follows a very similar trend. Near critical reflection in particular, all the wave energy that propagated from below as well as the energy extracted from the front, is dissipated. For example, we recover the fact that for $\overline{\text{Ri}} = 1.05$, $\max(R_{\mathcal{D}}) \approx 2$.

5. Discussion

Now that our analytical and numerical models have been validated, we can further explore parameter space to assess the robustness of the transfer of energy from balanced motions to waves near critical reflection.

a. Influence of the viscosity

One quantity, whose value is hard to constrain in the ocean, is the viscosity. To study the sensitivity of the energy ratios to the value of the viscosity, we now compute the analytical solution for $R_{\mathcal{E}}$ when ν is varied from 10^{-6} (molecular viscosity) to $10^{-3} \text{ m}^2 \text{s}^{-1}$.

Figure 9 shows that even if the viscosity is varied by three orders of magnitude, our main conclusions still hold both qualitatively and quantitatively, namely, critical and near-critical reflections induce energy transfers from the front to the waves and the maximum of $R_{\mathcal{E}}$ is of order one. Noticeable differences are that the lower the viscosity, the more peaked $R_{\mathcal{E}}$ is, indicative of a smaller band of frequencies in which viscous effects are important. As ν increases, the location of the peak of $R_{\mathcal{E}}$ shifts toward higher frequencies but remains near f .

There is a simple heuristic explanation as to why varying ν by orders of magnitude induces comparatively

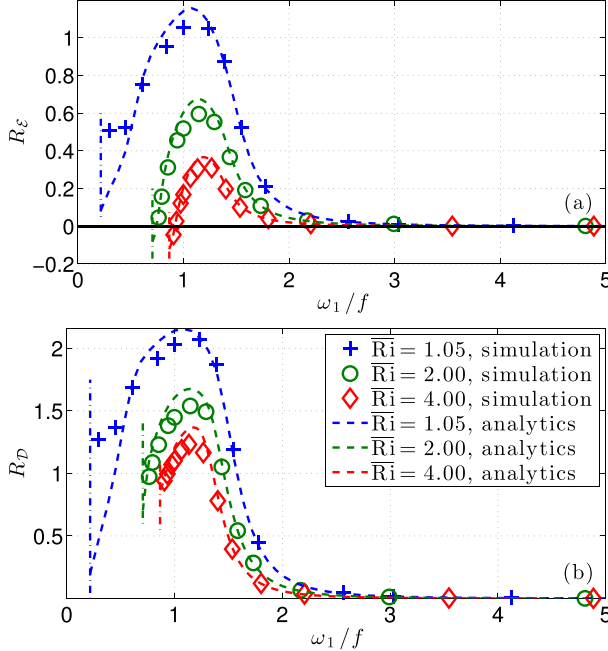


FIG. 8. As in Fig. 6, but for (a) exchange ratios R_ε and (b) dissipation ratios R_D as functions of ω_1/f and for three different Richardson numbers \bar{R}_i , diagnosed from linear simulations (markers) and analytical solutions (dashed lines), as calculated in sections 3c and 3d. The vertical dashed-dotted lines mark the minimum frequency ω_m for each \bar{R}_i .

modest modifications of R_ε . Reducing ν does not reduce the magnitude of the viscous dissipation because it also increases the intensity of the shear layers. Consequently, the dissipation occurs over a shorter depth and much more intensely since the amount of energy that is dissipated has to remain at least equal to the incoming energy flux at critical reflection.

b. Influence of the boundary condition on the buoyancy

We now change the boundary condition on the buoyancy [Eq. (20d)] to

$$\partial_z b|_{z=0} = 0, \text{ i.e. } \sum_{n=1}^5 \tilde{b}_n r_n = 0, \quad (32)$$

namely, a no flux boundary condition in which the isopycnals are free to be advected horizontally along the ocean surface. Figure 10 shows that changing the boundary condition leads to quantitative differences in the results; however, the order of magnitude of the energy exchange is preserved as well as its location and approximate shape of the $R_\varepsilon(\omega_1)$ curve. Therefore, our conclusions are not especially sensitive to the boundary condition on b .

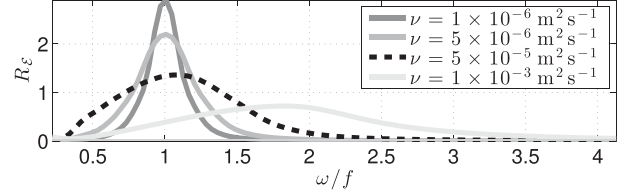


FIG. 9. Sensitivity of the exchange ratio R_ε to the viscosity ν , demonstrated with four values of ν . Note that the depth of the control volume V used in the calculation is $z_V = -50 \text{ m}$ instead of -25 m so that V encompasses the entire extent of the viscous solutions. The parameters used in the calculation are as in Fig. 4, except for the viscosity.

c. Nonlinear effects

When nonlinear terms are fully restored and wave-wave interactions are allowed ($\mathbf{u} \cdot \nabla \neq 0$), the exchange ratios R_ε are modified to different degrees depending on the frequency, as can be seen in Fig. 11. Specifically, the differences are strong for forward reflections, while linear and nonlinear backward reflections show essentially the same behavior. We recall from section 4a that $|m_1 U_1/N| = O(0.1)$, that is, the incident wave field has a small but finite amplitude. Table 1 contains all the actual amplitudes.

In GT15, we found that forward reflections differ qualitatively from backward reflections in that they favor nonlinear generation of higher harmonics (viz., waves of frequencies that are multiples of the wave maker frequency ω_1). Therefore, forward reflections can trigger a turbulent cascade, even for low incident wave amplitudes. We illustrate these differences in Fig. 12. Linear and nonlinear backward reflections seen in Figs. 12a and 12b are indeed very similar, which explains why R_ε is similar in both cases in Fig. 11. Figures 12c and 12d show that for critical reflection, nonlinear effects already significantly modify the flow and generate a signal that transports energy downward outside of V , away from the surface. This flow is described in great detail in GT15; its frequency content is mostly discrete and localized around frequencies that are multiples of the forcing frequency f . Each of these individual frequencies corresponds to a signal that is nonlinearly forced by nonresonant triads instead of being in the form of a freely propagating internal wave. Finally, in Figs. 12e and 12f, the differences between forward reflections are even more striking, with the linear case merely consisting of the superposition of an incident and a reflected wave, while the nonlinear case shows a turbulent field.

Nonlinear effects and turbulence can act to modify R_ε in different ways. For example, by generating waves with higher frequencies, and hence larger vertical group

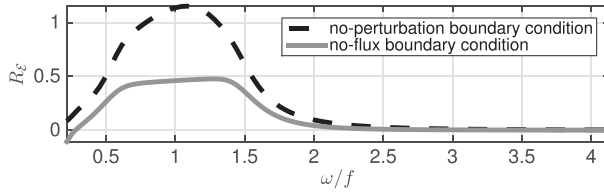


FIG. 10. Sensitivity of the exchange ratio R_E to the form of the boundary condition imposed on the perturbation buoyancy field at the surface, namely, $b|_{z=0} = 0$ (dashed) and $\partial_z b|_{z=0} = 0$ (solid). The parameters used in the calculation are the same as in Fig. 4.

velocities, more energy can be expelled out of the control volume V , preventing waves from exchanging energy with the front and therefore reducing the magnitude of R_E . This is clearly demonstrated in the nonlinear critical reflection simulation (1N010), in which the downward energy flux through $z = z_V$ associated with the signal visible in Fig. 12d was calculated to be $\langle(p + \mathcal{E}_h)w\rangle_{z=z_V}/\text{EF} - 1 = -0.286$, with EF being calculated using the dynamic pressure $p + \mathcal{E}_h$ associated with the incident wave [see Eq. (10)]. This number is close to the -0.247 reduction in R_E from 1L010 to 1N010 visible in Fig. 11.

On the other hand, the turbulence visible in Fig. 12f exhibits a continuum of spatial scales, which range from the size of the domain to the viscous dissipation scale. These small-scale structures propagate more slowly, are dissipated over shorter time scales, and therefore exchange more energy with the front. This is to be compared with the fast-propagating reflected waves of Fig. 12e, which leave the control volume V without significantly exchanging energy with the front. We can see in Fig. 11 that for $\omega_1 > 1.6f$, R_E is higher in nonlinear calculations, which suggests that in these cases, wave turbulence extracts energy from the front.

6. Conclusions

Near-inertial waves, propagating upward in a geostrophic front experience near-critical reflections when encountering the ocean surface (GT15). Viscosity modifies the polarization relations of steady-amplitude internal waves and allows for energy exchanges with the geostrophic front in nontrivial ways. In the present study, a vertical Laplacian was used as the frictional operator; other frictional operators will induce an energy exchange, albeit in a way that has to be quantified on a case-by-case basis. When nonlinear wave-wave interactions can be ignored, the reflected signal is described not by one reflected wave but by four solutions of the viscous equations of motion. The superposition of these solutions and their interactions leads to a net exchange of

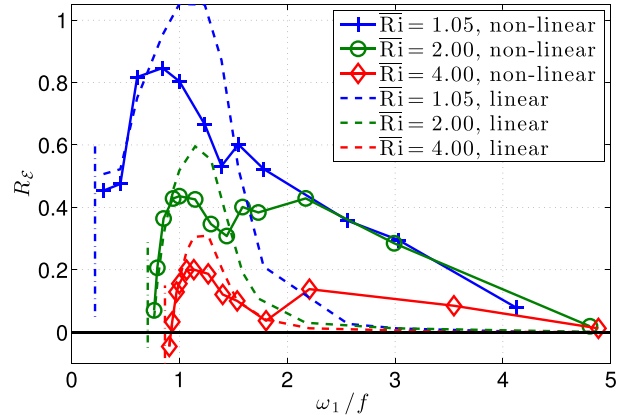


FIG. 11. As in Fig. 8a, but that the solid and dashed lines now represent the exchange ratio diagnosed from nonlinear (N) and linear (L) experiments, respectively. Namely, the dashed lines are the same as the crosses in Fig. 8a.

energy with the front, especially when the wave frequency is near critical. Away from critical reflection, waves simply reflect off the surface without experiencing such dissipative effects. Varying the viscosity and boundary conditions has a quantitative impact on the energy exchanges but does not change these conclusions. This extraction mechanism is specific to frontal critical reflection, as opposed to classical critical reflection on a slope where there is no background flow to extract energy from.

When nonlinear wave-wave interactions are allowed, these linear conclusions hold well for backward reflections ($\omega_1 < f$), since triadic resonances are not favored by such configurations (GT15). For this reason, this conclusion is likely to hold even for high wave amplitudes, provided that the incident or reflected waves are not individually unstable. On the other hand, when the reflections are forward, nonlinear wave-wave interactions can be close enough to triadic resonances to trigger a turbulent cascade, which strongly modifies the conversion of energy from geostrophic to ageostrophic motions. Possible explanations include the generation of high-frequency waves that propagate energy away from the surface and possibly away from the front and the generation of highly dissipating small scales that propagate more slowly, are dissipated more quickly, and therefore exchange more energy with the front. Because our non-dimensional wave amplitudes are relatively weak, this conclusion is once again likely to hold for a broad range of wave amplitudes, provided that they are large enough to be detectable but small enough to be stable.

The asymmetry between forward and backward reflections highlights the fact that nonlinear effects featured in forward reflection are crucial elements to the dissipation of frontal geostrophic energy. However, the

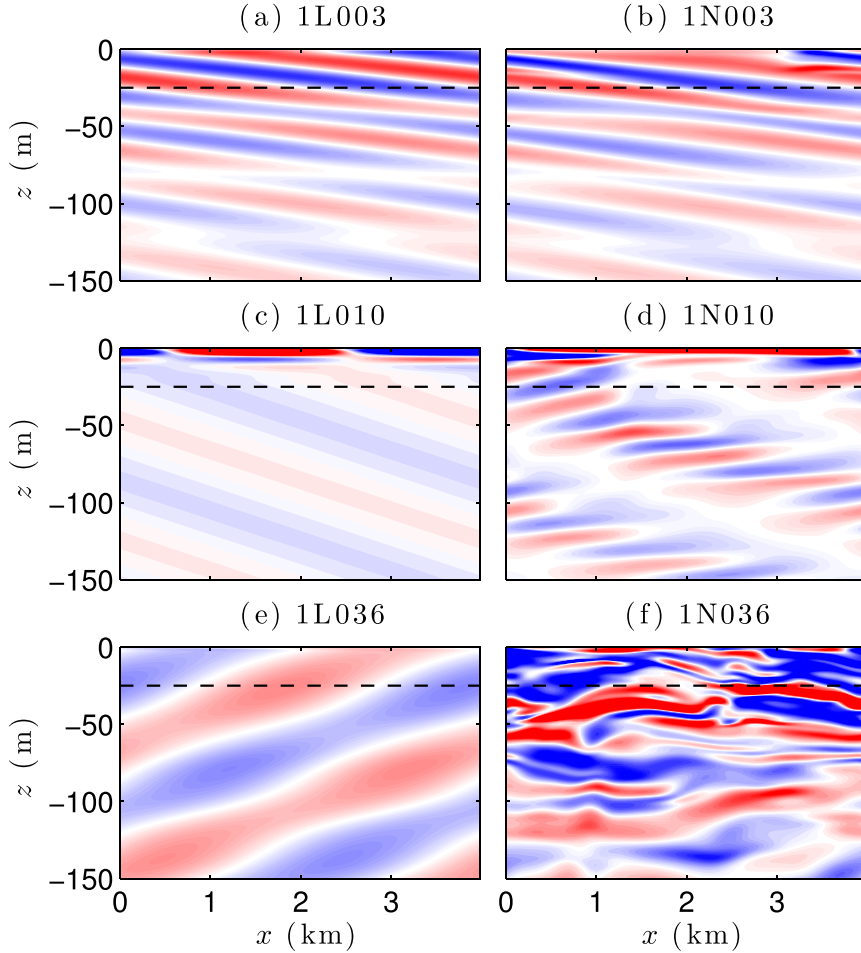


FIG. 12. Snapshots of the cross-plane vorticity $u_z - w_x$ in a few experiments with $\overline{\text{Ri}} = 1.05$, highlighting small-scale structures for (left) linear runs and (right) nonlinear runs and for (top) backward reflection ($\gamma = 0.3$ or $\omega_1/f \approx 0.45$), (middle) critical reflection ($\gamma = \omega_1/f = 1$), and (bottom) forward reflection ($\gamma = 3.6$ or $\omega_1/f \approx 3.0$). All color ranges are from -10^{-2} to $+10^{-2} \text{ s}^{-1}$, and the snapshots are taken at time $t = 20T_{\omega_1}$. The horizontal dashed lines are located at $z = z_V$, the lower bound of the control volume V .

two-dimensional nature of our experiments excludes other nonlinear effects that could influence wave-front energy exchanges. Further numerical work is therefore needed to quantify the role of, for example, three-dimensional frontal flows with strain and vertical vorticity that can significantly affect near-inertial waves (see Kunze 1985; Thomas 2012), three-dimensional (oblique) reflection (see, e.g., Thorpe 1999a,b, for classical critical reflection), or wave breaking, which is essentially a three-dimensional phenomenon (e.g., Lelong and Dunkerton 1998; Remmler et al. 2013).

By definition, critical reflection at fronts occurs immediately under the surface, where mixed layers are usually found. The question arises as to whether our results would still hold in the presence of a mixed layer. In the absence of hydrodynamic instabilities in the

boundary layer, such weakly stratified regions near the surface are necessarily characterized by low $\overline{\text{Ri}}$, which would presumably enhance the energy extraction from the fronts. But mixed layers are also dynamically active and critical reflection could be significantly modified by instabilities such as symmetric instability (SI) when $0 < \overline{\text{Ri}} \leq 1$ (Haine and Marshall 1998) or mixed layer baroclinic instability (MLI) when $\overline{\text{Ri}} > 1$ (Boccaletti et al. 2007). A common way to classify these instabilities is to characterize their associated energy transfers: SI extracts kinetic energy from the front, while MLI extracts potential energy. Our mechanism both extracts potential energy from and injects kinetic energy into the front, while consistently inducing a net extraction of energy from the front to ageostrophic motions. A major difference with SI or MLI, however, is that our

mechanism does not feature tracer transport at leading order. Indeed, internal waves are oscillations that, to the first order, do not advect tracers in a time-integrated sense. The wave-induced modification of the background flow that could arise from energy exchange during critical reflection could in turn rearrange scalar distributions of, for example, potential vorticity or nutrients but is only a second-order effect.

Relaxing the rigid-lid boundary condition could also introduce new and relevant physics. Direct free-surface effects are likely to be negligible: sea surface slopes due to geostrophic pressure gradients are usually much smaller than the $O(1\%)$ isopycnal slopes of strong fronts and the steep characteristic for $\omega = f$, while surface gravity waves oscillate too fast to directly affect such processes. However, indirect effects could be at play such as direct injection of turbulence in the dissipative boundary layer or Langmuir circulations generated by the surface gravity waves. As shown by, for example, Chini and Leibovich (2003) and Polton et al. (2008), the latter indeed have the potential to directly interact with internal waves and could once again modify the subsurface processes through which near-inertial waves dissipate their energy.

The present mechanism bears some resemblance with spontaneous wave generation [see the review of Vanneste (2013)], namely, it is also a wave–mean flow interaction problem in which waves remove energy from the geostrophic flow. Nonetheless, these two extraction mechanisms are very distinct in nature: while spontaneous generation depends on the Rossby number and results from the free evolution of a geostrophic flow, extraction due to critical reflection depends on the Richardson number of the geostrophic flow (Fig. 8) and is driven by a vertical energy flux associated with the inertial motions, which are imposed rather than develop spontaneously.

The present mechanism also bears some resemblance with the geostrophic to near-inertial transfer mechanisms of Gertz and Straub (2009) and Taylor and Straub (2016). Like us, they address interactions with externally forced near-inertial waves as the dominant mode of action of the near-inertial wave field on the geostrophic flow, rather than spontaneous loss of balance. However, their mechanisms act on gyrelike scales, the transfers happen mostly at the mesoscale rather than at the submesoscale (Taylor and Straub 2016), and it is nondissipative Reynolds stresses that carry out the transfers. Also, their numerical simulations lack some of the elements that could generate near-inertial waves propagating at the steep characteristic, as discussed in GT15. For

example, they do not feature bottom topography that is small enough to radiate lee waves (Nikurashin and Ferrari 2010) nor internal tides that could turn near-inertial if propagating toward high latitudes (Winters et al. 2011). The two mechanisms are therefore complimentary but distinct.

Finally, the recent study of Whitt and Thomas (2015) describes a distinct energy exchange mechanism in which inertial motions extract kinetic energy from the lateral shear of geostrophic flows, as opposed to the mechanism described in the present article, where the source of ageostrophic energy is dominantly the potential energy extracted from the lateral density gradient. For the mechanism of Whitt and Thomas (2015), the important parameter is the Rossby number and extraction scales with the wind work on inertial motions, while for critical reflection, the important parameter is the Richardson number and the extraction scales with the energy flux associated with the inertial motions. In the ocean, this energy flux can also scale with the wind work on inertial waves as well but not solely. A few alternatives discussed by GT15 include internal tides propagating poleward on a β plane that turn inertial when reaching their critical latitude (Winters et al. 2011), radiation of inertial waves by flows undergoing rapid evolution such as geostrophic adjustment (e.g., Blumen 2000; Plougonven and Zeitlin 2005) or frontogenesis (Shakespeare and Taylor 2014), and lee-wave instabilities radiating upward-propagating inertial waves (Nikurashin and Ferrari 2010; Rosso et al. 2015).

Acknowledgments. Support from the National Science Foundation through Grants 0961714 and 1260312 is acknowledged. Fruitful discussions with D. B. Whitt, R. M. Holmes, R. Pinkel, J. A. MacKinnon, M. H. Alford, T. M. S. Johnston, S. Taylor, and D. N. Straub are acknowledged.

REFERENCES

- Blumen, W., 2000: Inertial oscillations and frontogenesis in a zero potential vorticity model. *J. Phys. Oceanogr.*, **30**, 31–39, doi:[10.1175/1520-0485\(2000\)030<0031:IOAFIA>2.0.CO;2](https://doi.org/10.1175/1520-0485(2000)030<0031:IOAFIA>2.0.CO;2).
- Boccaletti, G., R. Ferrari, and B. Fox-Kemper, 2007: Mixed layer instabilities and restratification. *J. Phys. Oceanogr.*, **37**, 2228–2250, doi:[10.1175/JPO3101.1](https://doi.org/10.1175/JPO3101.1).
- Callies, J., R. Ferrari, J. M. Klymak, and J. Gula, 2015: Seasonality in submesoscale turbulence. *Nat. Commun.*, **6**, 6862, doi:[10.1038/ncomms7862](https://doi.org/10.1038/ncomms7862).
- Capet, X., J. C. McWilliams, M. J. Molemaker, and F. Shchepetkin, 2008: Mesoscale to submesoscale transition in the California Current System. Part III: Energy balance and flux. *J. Phys. Oceanogr.*, **38**, 2256–2269, doi:[10.1175/2008JPO3810.1](https://doi.org/10.1175/2008JPO3810.1).

- Chini, G. P., and S. Leibovich, 2003: Resonant Langmuir circulation–internal-wave interaction. Part 1. Internal wave reflection. *J. Fluid Mech.*, **495**, 35–55, doi:[10.1017/S0022112003006074](https://doi.org/10.1017/S0022112003006074).
- Colin de Verdière, A., 2012: The stability of short symmetric internal waves on sloping fronts: Beyond the traditional approximation. *J. Phys. Oceanogr.*, **42**, 459–475, doi:[10.1175/JPO-D-11-067.1](https://doi.org/10.1175/JPO-D-11-067.1).
- D’Asaro, E., C. Lee, L. Rainville, R. Harcourt, and L. Thomas, 2011: Enhanced turbulence and energy dissipation at ocean fronts. *Science*, **332**, 318–322, doi:[10.1126/science.1201515](https://doi.org/10.1126/science.1201515).
- Dauxois, T., and W. R. Young, 1999: Near-critical reflection of internal waves. *J. Fluid Mech.*, **390**, 271–295, doi:[10.1017/S0022112099005108](https://doi.org/10.1017/S0022112099005108).
- Ferrari, R., and C. Wunsch, 2009: Ocean circulation kinetic energy: Reservoirs, sources, and sinks. *Annu. Rev. Fluid Mech.*, **41**, 253–282, doi:[10.1146/annurev.fluid.40.111406.102139](https://doi.org/10.1146/annurev.fluid.40.111406.102139).
- Fox-Kemper, B., R. Ferrari, and R. Hallberg, 2008: Parameterization of mixed layer eddies. Part I: Theory and diagnosis. *J. Phys. Oceanogr.*, **38**, 1145–1165, doi:[10.1175/2007JPO3792.1](https://doi.org/10.1175/2007JPO3792.1).
- Gerkema, T., and V. I. Shrira, 2005: Near-inertial waves in the ocean: Beyond the ‘traditional approximation.’ *J. Fluid Mech.*, **529**, 195–219, doi:[10.1017/S0022112005003411](https://doi.org/10.1017/S0022112005003411).
- Gertz, A., and D. N. Straub, 2009: Near-inertial oscillations and the damping of midlatitude gyres: A modeling study. *J. Phys. Oceanogr.*, **39**, 2338–2350, doi:[10.1175/2009JPO4058.1](https://doi.org/10.1175/2009JPO4058.1).
- Grisouard, N., and L. N. Thomas, 2015: Critical and near-critical reflections of near-inertial waves off the sea surface at ocean fronts. *J. Fluid Mech.*, **765**, 273–302, doi:[10.1017/jfm.2014.725](https://doi.org/10.1017/jfm.2014.725).
- Haine, T. W. N., and J. Marshall, 1998: Gravitational, symmetric, and baroclinic instability of the ocean mixed layer. *J. Phys. Oceanogr.*, **28**, 634–658, doi:[10.1175/1520-0485\(1998\)028<0634:GSABIO>2.0.CO;2](https://doi.org/10.1175/1520-0485(1998)028<0634:GSABIO>2.0.CO;2).
- Joyce, T. M., J. M. Toole, P. Klein, and L. N. Thomas, 2013: A near-inertial mode observed within a Gulf Stream warm-core ring. *J. Geophys. Res. Ocean.*, **118**, 1797–1806, doi:[10.1002/jgrc.20141](https://doi.org/10.1002/jgrc.20141).
- Kunze, E., 1985: Near-inertial wave propagation in geostrophic shear. *J. Phys. Oceanogr.*, **15**, 544–565, doi:[10.1175/1520-0485\(1985\)015<0544:NIWPIG>2.0.CO;2](https://doi.org/10.1175/1520-0485(1985)015<0544:NIWPIG>2.0.CO;2).
- , and T. B. Sanford, 1984: Observations of near-inertial waves in a front. *J. Phys. Oceanogr.*, **14**, 566–581, doi:[10.1175/1520-0485\(1984\)014<0566:ONIWI>2.0.CO;2](https://doi.org/10.1175/1520-0485(1984)014<0566:ONIWI>2.0.CO;2).
- , R. W. Schmitt, and J. M. Toole, 1995: The energy balance in a warm-core ring’s near-inertial critical layer. *J. Phys. Oceanogr.*, **25**, 942–957, doi:[10.1175/1520-0485\(1995\)025<0942:TEBIAW>2.0.CO;2](https://doi.org/10.1175/1520-0485(1995)025<0942:TEBIAW>2.0.CO;2).
- Lelong, M.-P., and T. J. Dunkerton, 1998: Inertia–gravity wave breaking in three dimensions. Part I: Convectively stable waves. *J. Atmos. Sci.*, **55**, 2473–2488, doi:[10.1175/1520-0469\(1998\)055<2473:IGWB1T>2.0.CO;2](https://doi.org/10.1175/1520-0469(1998)055<2473:IGWB1T>2.0.CO;2).
- Molemaker, M. J., J. C. McWilliams, and X. Capet, 2010: Balanced and unbalanced routes to dissipation in an equilibrated Eady flow. *J. Fluid Mech.*, **654**, 35–63, doi:[10.1017/S0022112009993272](https://doi.org/10.1017/S0022112009993272).
- Mooers, C. N. K., 1975: Several effects of a baroclinic current on the cross-stream propagation of inertial–internal waves. *Geophys. Fluid Dyn.*, **6**, 245–275, doi:[10.1080/03091927509365797](https://doi.org/10.1080/03091927509365797).
- Nikurashin, M., and R. Ferrari, 2010: Radiation and dissipation of internal waves generated by geostrophic motions impinging on small-scale topography: Theory. *J. Phys. Oceanogr.*, **40**, 1055–1074, doi:[10.1175/2009JPO4199.1](https://doi.org/10.1175/2009JPO4199.1).
- Phillips, O. M., 1966: *The Dynamics of the Upper Ocean*. 1st ed. Cambridge University Press, 261 pp.
- Plougouen, R., and V. Zeitlin, 2005: Lagrangian approach to geostrophic adjustment of frontal anomalies in a stratified fluid. *Geophys. Astrophys. Fluid Dyn.*, **99**, 101–135, doi:[10.1080/03091920512331328080](https://doi.org/10.1080/03091920512331328080).
- Polton, J. A., J. A. Smith, J. A. MacKinnon, and A. E. Tejada-Martínez, 2008: Rapid generation of high-frequency internal waves beneath a wind and wave forced oceanic surface mixed layer. *Geophys. Res. Lett.*, **35**, L13602, doi:[10.1029/2008GL033856](https://doi.org/10.1029/2008GL033856).
- Rainville, L., and R. Pinkel, 2004: Observations of energetic high-wavenumber internal waves in the Kuroshio. *J. Phys. Oceanogr.*, **34**, 1495–1505, doi:[10.1175/1520-0485\(2004\)034<1495:OOEHIW>2.0.CO;2](https://doi.org/10.1175/1520-0485(2004)034<1495:OOEHIW>2.0.CO;2).
- Remmler, S., M. D. Fruman, and S. Hickel, 2013: Direct numerical simulation of a breaking inertia–gravity wave. *J. Fluid Mech.*, **722**, 424–436, doi:[10.1017/jfm.2013.108](https://doi.org/10.1017/jfm.2013.108).
- Rosso, I., A. M. Hogg, A. E. Kiss, and B. Gayen, 2015: Topographic influence on sub-mesoscale dynamics in the Southern Ocean. *Geophys. Res. Lett.*, **42**, 1139–1147, doi:[10.1002/2014GL062720](https://doi.org/10.1002/2014GL062720).
- Shakespeare, C. J., and J. R. Taylor, 2014: The spontaneous generation of inertia–gravity waves during frontogenesis forced by large strain: Theory. *J. Fluid Mech.*, **757**, 817–853, doi:[10.1017/jfm.2014.514](https://doi.org/10.1017/jfm.2014.514).
- Taylor, J. R., and R. Ferrari, 2009: On the equilibration of a symmetrically unstable front via a secondary shear instability. *J. Fluid Mech.*, **622**, 103–113, doi:[10.1017/S0022112008005272](https://doi.org/10.1017/S0022112008005272).
- Taylor, S., and D. N. Straub, 2016: Forced near-inertial motion and dissipation of low-frequency kinetic energy in a wind-driven channel flow. *J. Phys. Oceanogr.*, **46**, 79–93, doi:[10.1175/JPO-D-15-0060.1](https://doi.org/10.1175/JPO-D-15-0060.1).
- Thomas, L. N., 2012: On the effects of frontogenetic strain on symmetric instability and inertia–gravity waves. *J. Fluid Mech.*, **711**, 620–640, doi:[10.1017/jfm.2012.416](https://doi.org/10.1017/jfm.2012.416).
- , and P. B. Rhines, 2002: Nonlinear stratified spin-up. *J. Fluid Mech.*, **473**, 211–244, doi:[10.1017/S0022112002002367](https://doi.org/10.1017/S0022112002002367).
- , and J. R. Taylor, 2010: Reduction of the usable wind-work on the general circulation by forced symmetric instability. *Geophys. Res. Lett.*, **37**, L18606, doi:[10.1029/2010GL044680](https://doi.org/10.1029/2010GL044680).
- , and —, 2014: Damping of inertial motions by parametric subharmonic instability in baroclinic currents. *J. Fluid Mech.*, **743**, 280–294, doi:[10.1017/jfm.2014.29](https://doi.org/10.1017/jfm.2014.29).
- , A. Tandon, and A. Mahadevan, 2008: Submesoscale processes and dynamics. *Ocean Modeling in an Eddying Regime*, *Geophys. Monogr.*, Vol. 177, Amer. Geophys. Union, 17–38, doi:[10.1029/177GM04](https://doi.org/10.1029/177GM04).
- , J. R. Taylor, R. Ferrari, and T. M. Joyce, 2013: Symmetric instability in the Gulf Stream. *Deep-Sea Res. II*, **91**, 96–110, doi:[10.1016/j.dsr2.2013.02.025](https://doi.org/10.1016/j.dsr2.2013.02.025).
- Thorpe, S. A., 1999a: Fronts formed by obliquely reflecting internal waves at a sloping boundary. *J. Phys. Oceanogr.*, **29**, 2462–2467, doi:[10.1175/1520-0485\(1999\)029<2462:FFBORI>2.0.CO;2](https://doi.org/10.1175/1520-0485(1999)029<2462:FFBORI>2.0.CO;2).
- , 1999b: The generation of alongslope currents by breaking internal waves. *J. Phys. Oceanogr.*, **29**, 29–38, doi:[10.1175/1520-0485\(1999\)029<0029:TGOACB>2.0.CO;2](https://doi.org/10.1175/1520-0485(1999)029<0029:TGOACB>2.0.CO;2).

- , and A. P. Haines, 1987: On the reflection of a train of finite-amplitude internal waves from a uniform slope. *J. Fluid Mech.*, **178**, 279–302, doi:[10.1017/S0022112087001228](https://doi.org/10.1017/S0022112087001228).
- Vanneste, J., 2013: Balance and spontaneous wave generation in geophysical flows. *Annu. Rev. Fluid Mech.*, **45**, 147–172, doi:[10.1146/annurev-fluid-011212-140730](https://doi.org/10.1146/annurev-fluid-011212-140730).
- Whitt, D. B., and L. N. Thomas, 2013: Near-inertial waves in strongly baroclinic currents. *J. Phys. Oceanogr.*, **43**, 706–725, doi:[10.1175/JPO-D-12-0132.1](https://doi.org/10.1175/JPO-D-12-0132.1).
- , and —, 2015: Resonant generation and energetics of wind-forced near-inertial motions in a geostrophic flow. *J. Phys. Oceanogr.*, **45**, 181–208, doi:[10.1175/JPO-D-14-0168.1](https://doi.org/10.1175/JPO-D-14-0168.1).
- Winters, K. B., J. A. MacKinnon, and B. Mills, 2004: A spectral model for process studies of rotating, density-stratified flows. *J. Atmos. Oceanic Technol.*, **21**, 69–94, doi:[10.1175/1520-0426\(2004\)021<0069:ASMFPS>2.0.CO;2](https://doi.org/10.1175/1520-0426(2004)021<0069:ASMFPS>2.0.CO;2).
- , P. Bouruet-Aubertot, and T. Gerkema, 2011: Critical reflection and abyssal trapping of near-inertial waves on a β -plane. *J. Fluid Mech.*, **684**, 111–136, doi:[10.1017/jfm.2011.280](https://doi.org/10.1017/jfm.2011.280).